SAND2020-14339C

Rapidly Recovering Wind Turbine Wakes with Dynamic Pitch and Rotor Speed Control

Kenneth Brown[1], Daniel Houck[2], David Maniaci[3], Carsten Westergaard[4]
Sandia National Laboratories, Albuquerque, NM, 87123, U.S.A.

Advances in wind plant control have often focused on more effectively balancing power between neighboring turbines. Wake steering is one such method that provides control-based improvements in a quasi-static way, but this fundamentally does not change the downstream wake deficit and thus, can only provide limited improvement. Another control paradigm is to leverage the turbine as a flow actuator to dynamically excite unstable modes in the wake, thereby producing accelerated wake breakdown and recovery. Taking a more applied approach than some studies in the wake instability area, this article investigates the use of dynamic wake control (DWC) from two existing turbine control vectors, blade pitch and rotor speed, to incite rapid breakdown of the tip vortex structures. Both control vectors can be dynamically manipulated to make a significant difference on the wake structure and breakdown. The mid-fidelity free-vortex wake method (FVWM) used below allows a thorough search of the parametric space while still capturing the essential physics of the mutual inductance instability. The parameters for investigation include the frequency, amplitude, and phase of the harmonic forcing for both control vectors. The output from the FVWM is the basis for a Fourier stability analysis, which is used to pinpoint and quantify candidate forcing strategies with the highest instability growth rates and shortest near-wake lengths. The strategies, including dynamic rotor speed, blade pitch, and a novel tandem configuration, work to augment the initial tip vortex instability magnitude, leading to near-wake length reductions of greater than 80%, though without considering inflow turbulence. Analysis is provided to interpret these predictions considering the presence of inflow turbulence in a real atmosphere.

I. Introduction

A. Overview of Wind Turbine Wake Recovery

One of the largest remaining opportunities to reduce the levelized cost of wind energy will come from substantial gains in the understanding of complex wind plant aerodynamics and atmospheric phenomena, according to the U.S. Department of Energy [1]. As evidence, measurements over a range of modern wind plants across Europe [2] and in the U.S. [3] show that the second row of turbines in a wind plant captures around 20% less than power than the first when the turbines are aligned with the wind, and this falls to around 40% for turbines located deep within the array. In stable atmospheric conditions, even higher losses have been observed. Advances in wind plant layouts and wake steering techniques have improved plant performance, but the turbine spacing is still fundamentally constrained by the recovery of the turbine wake. In addition to this performance aspect, the turbulence of wakes significantly degrades the fatigue life of downstream turbines [4].

These problems can be traced back to the failure of the wake to fully "recover" from its depleted state after passing momentum to the turbine blades. During wake recovery, large-scale structures such as those produced by instabilities over a mixing layer entrain and inject a flux of mean-flow kinetic energy from the ambient flow into the depleted

[1] Postdoctoral Appointee, Wind Energy Technologies Department (kbrown1@sandia.gov).
[2] Postdoctoral Appointee, Wind Energy Technologies Department (drhouck@sandia.gov).
[3] Senior Researcher, Wind Energy Technologies Department (dcmania@sandia.gov).
[4] Senior Advisor, Wind Energy Technologies Department (chwest@sandia.gov).

wake. Most of this re-energizing occurs in the far-wake, which begins somewhere between two and four diameters downstream from the turbine [5, 6].

In the near wake, there exists a rich mix of relatively organized flow features that propagate downstream of a turbine. These coherent features include a region of velocity deficit on the scale of the rotor diameter, swirling motion opposite the blades' rotation direction, an initially two-dimensional wake structure from the tower shadow, helicoidally-tracking vorticity (tip, root, and shed components), a columnar hub vortex, lateral spreading due to a pressure differential with the ambient flow, and entrainment of ambient flow promoting wake recovery, as well as any features that might be recognizable from the atmospheric boundary layer (ABL) inflow. Lignarolo *et al.*'s [7] measurements showed that, within the near wake, the flow across the shear layer is governed by the periodic tip vortex structures and results in a roughly zero net recovery of mean-flow kinetic energy, the helical tip vortices effectively shielding the wake from the ambient flow. Speeding the transition to the far wake via the breakdown of the tip vortices is thus critical for wake recovery.

B. Inherent Wake Instabilities

The transition between near-wake and far-wake regions is triggered by instabilities in the wake and resulting breakdown of the tip vortices [8, 9]. Theoretical analysis of tip vortex stability offers three instability mechanisms: short-wave sinuous instability, long-wave sinuous instability, and mutual inductance instability [10]. The short-wave instability is due to the self-inductance of nearby locations on the vortex filament and results in localized "squiggles" along the filament. The long-wave instability is related to interactions between neighboring filaments that, when allowed to amplify, result in the mutual inductance (vortex pairing) instability [11] and the eventual "leapfrogging" of one vortex by another. It is this latter instability that has been shown to be the dominant cause of the beginning of wake breakdown in wind turbines [7, 9, 12], propellers [8], and hovering rotors [13]. An excellent experimental flow visualization of the process was given by Alfredsson and Dahlberg [14] as shown in Figure 1, along with a comparable lifting line free-vortex method result from Marten *et al.* [15].

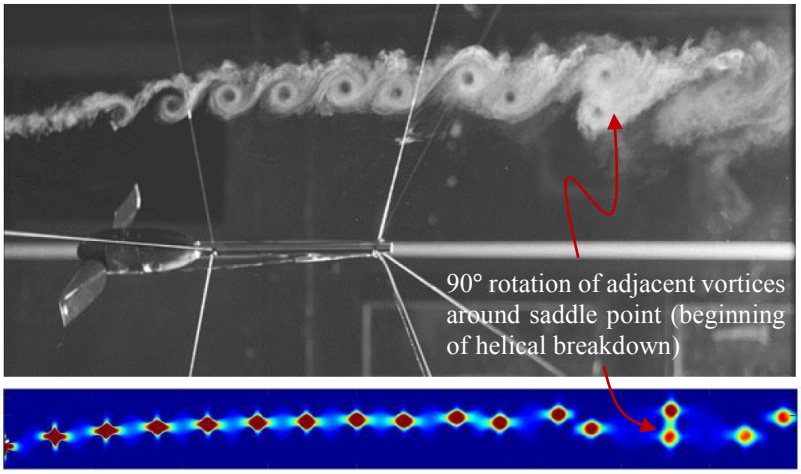

Figure 1. Progression of a mutual inductance instability, or leapfrogging, event for tip vortices. Top: Smoke visualization of the tip vortex from a two-bladed scaled model. Reproduced from [14]. Bottom: Snapshot of Q-criterion from a lifting line free vortex method. Reproduced from [15].

It is well documented that the location of the breakdown is a function of the spacing between consecutive tip vortex spirals that, in turn, is a function primarily of thrust coefficient and number of blades [8, 16, 17]. Furthermore, recent experiments spanning a range of (diameter) Reynolds numbers from approximately 90,000 to 40,000,000 (or 40M), and related both to wind energy [18, 19] and propulsion [20], have validated that the streamwise distance before vortex breakdown (and therefore the beginning of the wake recovery) is inversely proportional to the level of external disturbance via turbulence. The hub vortex also plays a role in the tip vortex evolution as it has a stabilizing effect on the tip vortices. However, the hub vortex is more short-lived than the tip vortex and therefore does not likely contribute to the tip vortex breakdown [8, 17] (the results of [8], at least, imply that the tip vortex destabilizes the hub vortex rather than vice-versa).

Several studies have demonstrated that the modes of the mutual inductance instability that result in maximum exponential growth correspond to half integer multiples of the number of blades (i.e., the disturbance of every other helical vortex is 180 degrees out of phase) [16, 17, 21]. The nondimensional wavenumber, ω, for each of these modes is the number of perturbation periods per rotor revolution as given by Equation 1 [16]

$$\omega = N_b(k - 0.5), \quad (1)$$

where N_b is the number of turbine blades and k are positive integers (note that some references such as [11] use an alternate convention so that the quantity in the parenthesis is simply k). The $k = 1$ mode has been found to be primarily responsible for the transition to the non-linear instability growth regime that is characteristic of the beginning of the wake breakdown process [17]. This instability is evident mainly in the axial and radial directions, and the displacements in these directions are of the same order but 180 degrees out of phase. Because of the phase difference, axial movements of a vortex filament towards its upstream neighbor coincide with the neighbor's downstream movements, thus resulting in imminent pairing, after which the phase shift discontinues. Given knowledge of the dominant instability modes, a logical next step forward for wind energy applications is to explore how these modes can be excited to promote wake breakdown.

C. Intentional Wake Forcing

While many wind plant optimization studies focus on moderating the power extraction of "greedy" upwind turbines to yield a net plant-wide gain or on steering the wake of upstream turbines to avoid downstream ones, a different and ultimately more appealing strategy is to reduce the length of the wake recovery process. Since this recovery process siphons energy from the canopy above into the far wake below, speeding the onset of the far wake effectively increases the capture area of a wind plant with high power density. One avenue to accomplish this goal involves altering the blade induction distribution to speed the wake mixing process [22], though modification of the blade design does not allow any real-time control authority, besides via different combinations of collective pitch and rotor speed.

A more flexible approach has come into the spotlight in the last several years: dynamic forcing of the wake to excite the instability modes. Much of the work has dealt with forcing frequencies that are appropriate for exciting bluff-body-type instabilities [23-26]. Another dynamic forcing strategy, and one with possibly more potential, is forcing of the mutual inductance instability described above using the triggering frequencies determined by Equation 1.

Despite strong literature contributions on the physics of the growth of the mutual inductance instability as reviewed above, relatively few studies have applied this knowledge and attempted to *excite* the instability. Several exceptions are described here. Following the numerical work of Ivanell *et al.* [17], Odemark and Fransson [27] demonstrated on a scaled wind turbine that the tip vortex pairing processes is affected by periodic forcing from pulsed jets emanating from the hub into the wake. The vortex pairing process, which was observed to occur between 1-2.5D from the rotor, was associated with a shift in energy from the blade passing frequency to a lower frequency depending on the initial vortex strengths of the tip vortices trailing from each blade. Quaranta *et al.* [11], with a slightly more applied approach, modulated the rotor speed of a single-bladed scaled model and demonstrated that the leapfrogging position (*swapping* position in their notation) decreases by 60% as the initial tip axial displacement amplitude is increased from 1% to 15% of the distance between adjacent helices. Marten *et al.*'s [15] lifting-line free-vortex wake method also predicts a roughly 60% reduction in near-wake length by harmonic actuation of outboard flaps at an amplitude of 10°. The dynamic wake forcing strategies leveraged by Odemark and Fransson [27] and Quaranta *et al.* [11] were conducted in low turbulence environments with $\leq 1\%$ ambient turbulence intensity. Wake forcing is likely to be most successful in lower turbulent environments, such as stable ABLs, where periodic forcing can compensate for the lack of natural unsteadiness to augment the initial instability magnitude. Marten *et al.*'s [15] results were made with 10% inflow turbulence intensity, though their wake modeling ignored interaction between the original freestream vortices and the added wake ones.

Following in the path of the work above, the present study offers to quantify the benefit of optimal forcing strategies that encourage wake recovery. The innovative aspects of the work stem from the application of forcing using control vectors, blade pitch and rotor speed control (both individually and a novel tandem configuration), that are already available on all modern wind turbines. In contrast to the limited cases where such control vectors have been studied previously for their potential to excite the mutual inductance instability, i.e., [11], the computational approach below permits more thorough exploration of the parametric space than was previously possible.

The formulation of the so-called dynamic wake control (DWC) waveforms is given in Section II. Section III describes the computational approach, which is enabled by multi-threaded parallel computing combined with mid-fidelity modeling that captures the essential physics relevant to vortex instability. Section IV details results of parametric studies of forcing frequencies, amplitudes, and phases of the harmonic control actions. For each flow

simulation, a Fourier stability analysis will offer insight on the instability growth rates and resulting near-wake lengths. Section V compares the effects of the DWC-induced instabilities with those of natural turbulent inflow, and concluding remarks are made in Section VI.

II. Dynamic Control Strategies

The DWC strategy is to introduce an oscillation to the wake flow at an appropriate wavenumber to amplify the existing tip vortex instability and accelerate wake breakdown and recovery. Three control vectors exist on typical full-scale turbines: yaw, collective pitch, and rotor speed. State-of-the-art wake steering is based on quasi-static yaw offsets attempting to steer wakes away from downstream turbines. However, typical yaw rates of large turbines (0.3°/s for the NREL 5MW [28]) are too slow to achieve any kind of meaningful oscillation amplitude that would be needed to gain active DWC authority at even the lowest k in Equation 1. In addition, the mechanical wear on the yaw actuation system is unfavorable. On the other hand, both the blade pitch rates (8°/s for the NREL 5MW [28]) and the generator speed control (almost instantaneous response) provide ample authority for DWC strategies given a relatively steady inflow where the dominant timescales of the flow, and thus of the conventional control signals, are large with respect to the rotor period. Adjusting the rotor speed additionally gives the upside that the pitch system duty cycle, which is a common weakness, does not increase. However, torsional fatigue loads would go up to some extent on the drivetrain, which has yet to be evaluated.

For the DWC approach presented below, the dynamic pitch setting, p, (an increase in p corresponds to a reduction in blade angle of attack) relative to that of the conventional control setting, p_0, is described by the equation

$$p = p_0 + a_p \sin(\omega_p \theta + \phi_p), \tag{2}$$

where a_p indicates the dynamic pitch amplitude, ω_p is the angular perturbation wavenumber described in Equation 1, θ is the rotor azimuthal angle, and ϕ_p is any phase offset. The dynamic rotor rotational frequency, f, relative to that of the conventional control setting, f_0, is described by the equation

$$f = f_0 + a_f \sin(\omega_f \theta + \phi_f), \tag{3}$$

where the subscript f is used to now distinguish between variables of the same names from Equation 2.

III.Computational Setup

A. Reference Turbine

An example case of DWC is demonstrated with the NREL 5MW reference turbine [28]. The 126 m diameter turbine is operated at rated conditions with a uniform freestream velocity of 11.13 m/s, rotation rate of 12.1 rpm (tip speed ratio of seven), and blade pitch of zero degrees. The airfoil data for the turbine come from the two-dimensional polars of [29], and no corrections are yet made for three-dimensional effects. The spanwise arrangement of the eight airfoils into 17 spanwise segments as well as the variation in chord and twist along the blade span are given in [28].

Differentiating Equation 2 with respect to time and considering the maximum pitch rate of 8°/s for the NREL 5MW, the maximum a_p attainable is 4.2° for the $k = 1$ case at the above rotation rate. The authors are unaware of limits on the rate of rotor speed modulation other than due to the bounds of the torque capabilities of the generator and the drive train.

B. Mid-Fidelity Aerodynamic Model

1. First-Order Estimation Using Free-Vortex Wake Methods (FVWMs)

FVWMs are mid-fidelity aerodynamic simulations that are founded on the assumption that the regions of viscous-induced vorticity in the flow are concentrated to relatively small length scales. This allows the vorticity to be appropriately modeled as distributed singularities, and the viscous diffusion term can be dropped from the PDE of vorticity transport. By consideration of the vorticity transport PDE and Helmholtz's second law, the simple advection

equation can be found that underlies the FVWM approach, which includes the time-rate of change of the position vector of a Lagrangian marker (vortex segment) on the left-hand side and the sum of all the Biot-Savart-induced velocities and freestream velocity on the right-hand side [13]. Second-order accuracy of both sides of the advection equation can be achieved given an appropriate finite differencing scheme and a rotor angular discretization of less than 2.5-5° [30].

Vortex methods are well suited for the present analysis, given that atmospheric effects are not modeled at this stage of the work. The simplified modeling of viscous effects is of relatively small consequence for the problem at hand as the mutual inductance instability is an inviscid phenomenon, and the flow regime is of high Reynolds number. The FVWM is furthermore convenient for the present analysis because it allows explicit tracking of the vortex filament locations. Lastly, the computational efficiency of a FVWM allows thorough exploration of parametric spaces that is not typically feasible on state-of-the-art actuator line large-eddy simulations, which have computation times of 4-5 orders of magnitude greater than FVWMs [15].

The effectiveness of FVWM tools for analysis of tip vortex stability was illustrated by several studies [15, 16, 21, 31]. The first application was in the field of rotorcraft; see Bhagwat *et al.* [16]. These authors used the steady-state solution of a FVWM as the basis for a linear eigenvalue stability analysis that identified the $\omega = 0.5N_b$ instability mode as having highest amplification. For wind energy applications, Rodriguez and Jaworski [21], Rodriguez *et al.* [31], and Marten *et al.* [15] also performed stability analyses on FVWM wakes but with time-marching rather than steady-state solutions being used to capture realistic transient wake geometries associated with floating offshore turbines, flexible blades, and flap actuation control, respectively.

Bhagwat *et al.* [16] also provided a cautionary note on using FVWM to study stability; numerically-induced instabilities can be significant and can undo a FVWM's second-order accuracy if not contained. For the time-marching methods that are required to model transient effects, the truncation error of higher-order terms in the explicit solution is an inevitable source of artificial instability. Other errors due to wake discretization, wake truncation, and viscous core models may be present in both time-marching and relaxation methods. These non-physical instabilities should be in general minimized as they may obfuscate the fluid dynamic instabilities of interest. Fortunately, given that a FVWM's discretization is consistent with the governing equation of motion, convergence of the wake solution with increasing grid refinement is sufficient to demonstrate numerical stability. This requirement was met with an azimuthal step size of 5° for a time-marching algorithm in [30].

It is inevitable that some numerical instability will remain. In a conventional FVWM without DWC, small numerical instability is in fact required to initially excite unstable modes from their state of (unstable) equilibrium [30], since FVWMs generally do not feature the inflow turbulence that is responsible for perturbing tip vortex instabilities in the natural atmosphere. However, a difference in the character of the initial perturbation is likely to exist between the perturbations provided by the numerical instabilities and those of a real turbulent atmosphere. Thus, some FVWM predictions are less reliable in terms of the absolute locations of vortex pairing (which depend on the magnitude of the initial perturbation) [16], but the *relative* rates of disturbance growth predicted between different solutions in a parametric study are valid. In our study, much of this concern is minimized because the magnitudes of the DWC-induced perturbations are generally much larger than those of the artificial perturbations.

Other modeling limitations of FVWMs are the limitation to uniform inflow profiles, in general, since sheared inflow profiles have shown non-physical results [32] and the loss of accuracy after vortex pairing since turbulent mixing is not properly modeled. Effects of the former are not considered here though described in [33], and errors from the latter are of minimal relevance to the present study that is concerned with only the initial vortex pairing process.

2. *FVWM Baseline Implementation*

In this work we use the FVWM Code for Axial and Cross-flow TUrbine Simulation (CACTUS) developed at Sandia National Laboratories for the study of wind and water turbines [34]. The code uses a second-order predictor explicit time advancement scheme with a lifting line solution for the blades and a lattice for the free wake. For the lifting line, circulatory unsteady effects for attached conditions are handled using the pitching flat plate analogy. Furthermore, two dynamic stall models are available in CACTUS, and we use the modified Boeing-Vertol model for all results below unless otherwise noted. For the free wake, uniform or linearly varying velocity profiles model the vortex cores, the former being employed in this work. Ground and tower effects can be modeled in CACTUS though are ignored presently. The current work is enabled using the OpenMP interface within CACTUS, and this capability may also benefit future studies involving larger numbers of simulations towards further detailed parameter sweeps of different DWC waveforms, frequencies, amplitudes, and duty cycles.

The case inputs for the CACTUS runs follow from the rated conditions, as well as the turbine and blade geometry, which were introduced in Section III.A. Note that the same spanwise discretization of the 17 aerodynamic stations for the NREL 5MW have been used successfully in previous FVWM tip vortex stability analyses [21, 31, 35].

The configuration inputs for the CACTUS runs are held at the default settings defined in [34] except for the following. The number of iterations between wake convection velocity updates is enforced to remain at one. The number of azimuthal steps per rotor revolution was determined from the convergence study illustrated by Figure 2. For all revolution counts studied, the revolution-averaged power coefficient, C_p, (standard definition as described in [34]), converged to well within 10^{-3} by $2\pi/\Delta\theta$ =80 (azimuthal step size, θ, of 4.5°), where convergence at each revolution count is assessed relative to the C_p of a reference simulation at $2\pi/\Delta\theta$ =120 (θ =3°) and the same revolution count. As 80 azimuthal steps per revolution not only achieves independence from the azimuthal resolution as shown in Figure 2 but also ensures second-order accuracy of the reconstructed velocity field [13], this step size was used for all subsequent simulations. Furthermore, the absolute C_p was found to be sufficiently converged by 32 revolutions, which is thus taken as the precursor simulation length for all subsequent simulations. For all simulations including the convergence study, wake points beyond four diameters downstream from the rotor plane were ignored for efficiency, a simplification that will produce less than 1% error in absolute C_p according to analysis based on [36].

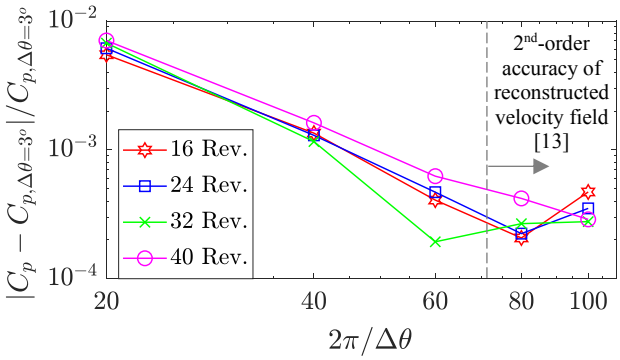

Figure 2. Convergence study of revolution-averaged turbine power coefficient, C_p, with increasing number of azimuthal steps per revolution, $2\pi/\Delta\theta$. Different numbers of total revolution counts are indicated in the legend. Each C_p is referenced to the C_p for the $2\pi/\Delta\theta$ = 120 ($\Delta\theta$ = 3°) case with the same respective number of total revolutions.

The data output from CACTUS occurred during revolutions 33-34 of the simulation, during which the velocity field was evaluated every two azimuthal steps on a three-dimensional grid of size 50 by 100 by 100 over the domain ranges of $0 \le x/D \le 5$, $-0.7 \le y/D \le 0.7$, and $-0.7 \le z/D \le 0.7$, respectively. The vortex filament positions and velocities were also saved during these final two revolutions.

The baseline case of the FVWM simulation without dynamic forcing is shown in Figure 3. In accordance with the "horseshoe" type vortex structure of vorticity typically observed on rotors, the trailing vorticity of the blades is primarily contained in the filaments at the extremes of the blade spans with opposite sense of rotation at each extreme. As introduced in Section I.B, we are primarily concerned with the tip vortex filaments, and it is apparent that both of the two outermost filaments emanating from each blade contain significant circulation. The separation of the trailing tip circulation into two distinct regions of concentrated circulation is due to the spanwise numerical discretization of the shed vorticity. Furthermore, the axial separation of two adjacent tip helices, h, (see Figure 3) is around 10 times greater than the radial separation of the two outermost filaments in a helix sheet in our current modeling approach, so any given axial pair of outer filaments may be considered to be in the far-field of the circulation field of tip filament pairs on neighboring helix sheets.

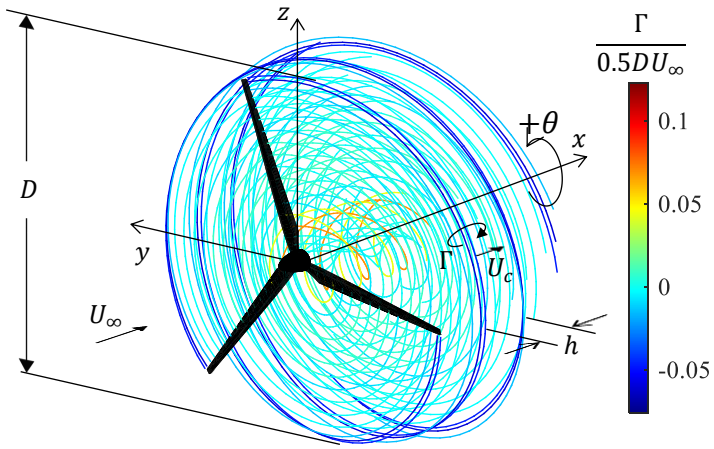

Figure 3. Trailing vortex filaments from a baseline simulation with no dynamic forcing. The filament color indicates normalized circulation, Γ. Plotted data are restricted to one revolution for clarity. Trailing filaments only are shown without the spanwise filaments. Rotor geometry is for visual reference only and not representative of the NREL 5MW used in the simulations.

Consequently, the circulation from the outermost two filaments of a helix sheet will be lumped together when calculating the tip circulation to be used to normalize instability growth rates below.

3. FVWM Modifications

The code used in this work is a modified version of CACTUS that allows for dynamic actuation of blade pitch and rotor speed. The actuation is accomplished by updating the blade pitch and/or rotor speed at each azimuthal station according to Equations 2 and 3. The inputs for both actuation types thus include the frequency, amplitude, and phase offset of the control waveform. To verify the correctness of the coding modifications, traces of the quarter-chord angle of attack and local velocity at the blade from the modified CACTUS output, after removal of the induced velocity components, were found to match those implied by Equations 2 and 3. Code modification has also been made to output velocity field data in the rotating frame of reference rather than the fixed frame of reference to aid the stability analysis to follow.

The unsteady forcing is applied for the full 34 revolutions of the simulation. It should be mentioned that rotor inertia is not considered, and that blade pitch and rotor speed have no interaction with one another as implemented. The effects of rotor inertia, blade aeroelasticity, drivetrain dynamics, and pitch-speed interaction will be investigated in future work but were deemed secondary in attempting to establish the overall control method feasibility.

C. Fourier Stability Analysis

Previous work has found success using wake data from a variety of sources including FVWMs as the basis for both linear eigenvalue stability analyses [16, 21, 31] and Fourier analyses [15, 17, 27, 33] of tip vortex divergence rates. Below, we leverage both to demonstrate the effects of dynamic control actions on wake instability and near-wake length, though the Fourier analysis is used predominantly and is therefore the only one outlined in this section. Previous authors have implemented Fourier stability analyses by either extracting the maximum response of the frequency of interest (FOI) from the Fourier spectra at each cross-section [17, 33], or by integrating over the region of tip vorticity at the FOI [15] or over a band of frequencies centered around the FOI [27]. Here, we follow closely the approach of Ivanell *et al.* [17].

Time-resolved cross-stream flow snapshots in the rotating frame of reference are temporally mean-subtracted to give the field of the fluctuating velocity component, $\boldsymbol{u}'_n$, across each snapshot, n. The $\boldsymbol{u}'_n$ are transformed into the frequency domain to yield the Fourier coefficient, $\widehat{\boldsymbol{u}}'_j$, via Equation 4

$$\widehat{\boldsymbol{u}}'_j = \frac{1}{N}\sum_{n=0}^{N-1} \boldsymbol{u}'_n \, e^{-i2\pi jn/N} \,, \tag{4}$$

where N is the total number of snapshots and j is the index of the integer-valued mode numbers from 0 to $N/2-1$ with corresponding frequencies given by $f_j = j/(N\Delta t)$ where Δt is the time step between successive snapshots. The most unstable location within the annulus defined by $0.375 \leq r/D \leq 0.625$ for each yz plane is $|\widehat{\boldsymbol{u}}'_j|_m$, which is calculated according to Equation 5

$$|\widehat{\boldsymbol{u}}'_j|_m = \max_{yz} |\widehat{\boldsymbol{u}}'_j| \,, \tag{5}$$

where $r = \sqrt{y^2 + z^2}$ and the $|\cdot|$ notation denotes the magnitude of a complex quantity. For numerical reasons, the location of $|\widehat{\boldsymbol{u}}'_j|_m$ at different axial locations may alternate between the three regions corresponding to the tip vortex filaments trailing from each of the three blades. Note that the practice of taking the maximum of $|\widehat{\boldsymbol{u}}'_j|$ at each j contrasts with the approach of Ivanell *et al.* [17] who took the y- and z-coordinates of $|\widehat{\boldsymbol{u}}'_j|_m$ for the $k = 1$ case as the coordinates for the $|\widehat{\boldsymbol{u}}'_j|_m$ of all the remaining k cases. Note that in some cases below, the index j will have a subscript of its own to denote a specific k frequency parameter of interest. For instance, $|\widehat{\boldsymbol{u}}'_{j_1}|_m$ refers to the $k = 1$ case.

The increase of $|\widehat{\boldsymbol{u}}'_j|_m$ along the streamwise direction serves as an indicator of the growth of instabilities for each frequency component. Specifically, the ratio of $|\widehat{\boldsymbol{u}}'_j|_m$ between two streamwise locations can be related to the temporal growth rate of an instability, σ. The growth relationship takes the form of an exponential function in accordance with known character of the mutual inductance instability within its linear growth region [9, 17] (the linear region refers to that which shows linear growth using semi-log plotting; see Figure 4 further below). Equation 6 gives this relationship

$$|\hat{\boldsymbol{u}}_{j,2}^{'}|_m \,/|\hat{\boldsymbol{u}}_{j,1}^{'}|_m \;= e^{\sigma(x_2-x_1)/U_c}\,, \tag{6}$$

where U_c is the convection velocity of the tip vortices obtained by extracting the axial velocity of the vortex filaments within the linear region of growth from the FVWM results, and the subscripts "1" and "2" indicate two different axial locations in the flow field. By performing linear regression on the linear growth region, σ is thus identified. The non-dimensionalization of σ into σ^* is accomplished according to Equation 7 [11]

$$\sigma^* = \sigma \times 2h^2\Gamma^{-1}\,, \tag{7}$$

where h is taken as a close approximation for the perpendicular distance between two consecutive filaments, and Γ is the circulation of the filaments. Strictly speaking, the oft-quoted maximum non-dimensional growth rate of $\sigma^* = \pi/2$ applies only to an infinite row of identical point vortices. For the more realistic case of a periodic array of inclined straight vortices, the value of σ^* for the NREL 5MW at rated conditions is only 0.2% greater than the point vortex value for $k = 1$ according to the derivation of Quaranta *et al.* [11].

Before coming to the parametric studies and physical interpretations of the effects of control vectors in the following section, we here present the Fourier analysis as applied to an example wake with dynamic forcing to point out several key features of the Fourier analysis output. The control vector in this example case is rotor frequency, which is prescribed from Equation 3 using $a_f = 0.02$ rpm, $\omega_f = 1.5$ rad^{-1} ($k = 1$), and $\phi_f = 0°$. Figure 4(a) describes the streamwise growth of the scaled and normalized tip vortex instability magnitudes at five k values including the forced frequency at $k = 1$. In the axis label as well as all following occurrences, division of $|\hat{\boldsymbol{u}}_j'|_m$ by a reference value of 1 m/s is assumed to make the quantity inside the natural logarithm dimensionless. The $|\hat{\boldsymbol{u}}_j'|_m$ are furthermore normalized before plotting to compare with the maximum non-dimensional rate predicted by the classical $\pi/2$ vortex pairing result as described earlier. Normalization values derive from the linear region of the baseline solution without any DWC where $h = 14.1$ m, $U_c = 8.60$ m/s, and $\Gamma = 76.2$ m^2/s, the former two being calculated as the mean between the two outermost filaments in a helix sheet and the latter as the sum over the two outermost filaments as described

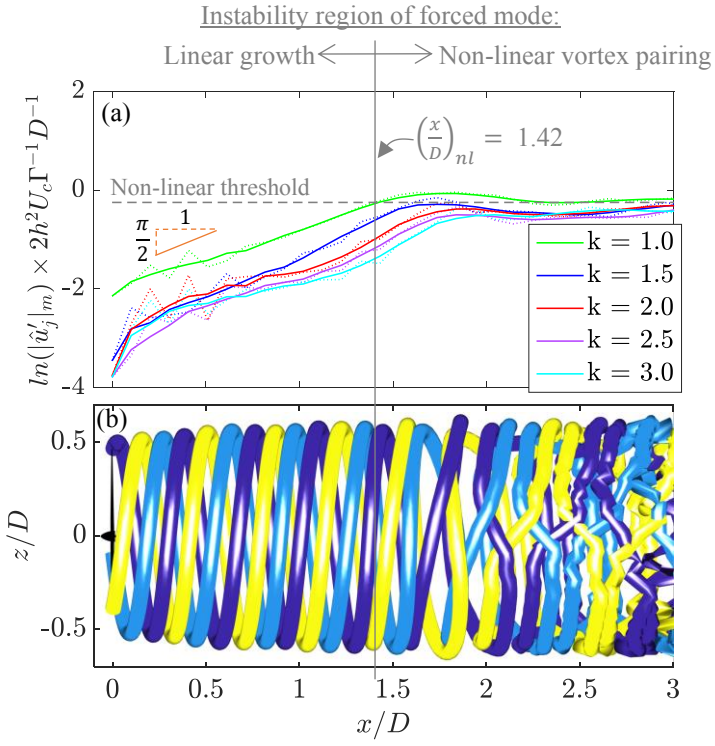

Figure 4. (a) Maximum wake instability Fourier coefficients, $|\hat{\boldsymbol{u}}_j'|_m$, at each streamwise coordinate, x/D, for $a_f = 0.02$ rpm, $\omega_f = 1.5$ rad^{-1} ($k = 1$), and $\phi_f = 0°$. The dotted lines represent raw $|\hat{\boldsymbol{u}}_j'|_m$ while solid lines are the moving average of the raw data taken with a window size of five points. Normalization values are provided in the text. (b) Trajectories of the outermost tip vortex filaments at an instant in time from the simulation in (a). The filament diameter does not possess meaning and is only scaled for visual clarity in this figure.

previously. Smoothing of $|\widehat{\boldsymbol{u}}_j'|_m$ is applied with a moving average taken with a window size of five points, and this smoothing helps to account for variation in $|\widehat{\boldsymbol{u}}_j'|_m$ due in part to finite output grid resolution. Only the smoothed and not the raw results are shown in the remainder of the figures.

After an initial period of receptivity, the growth rate for the $k = 1$ forcing frequency remains close to the theoretically predicted $\sigma^* = \pi/2$ maximum until the non-linear region is reached at $x/D \approx 1.42$, wherein the flattening of the growth represents the onset of the tip vortex pairing and breakdown event [17]. Finally, at around $x/D \approx 1.75$, the mutual inductance instability growth sees adjacent helices leapfrog one another. The leapfrogging event can be observed directly from view of the outermost vortex filaments themselves in Figure 4(b). Rather sudden disorganization of the flow occurs within $1D$ of the vortex breakdown. Similarly to [17], we consider in this work the end of the near wake to be the location of a non-linear threshold, which in our case is $ln(|\widehat{\boldsymbol{u}}_j'|_m) \times 2\, h^2\, U_c\, \Gamma^{-1}\, D^{-1} =$ -0.25.

The other k values besides the forced $k = 1$ case, which in the case of Figure 4(a) are all harmonics of the forcing case, show fast initial growth before eventually attaining nearly the same growth rate, though not the same magnitude, as the forced case. The non-forced k cases will not be plotted in the remainder of the article.

IV. Stability Results

This section gives the Fourier analysis results on the sensitivity of the wake instability growth to three dynamic forcing parameters: frequency, amplitude, and phase. A subsection is devoted to each parameter.

A. Frequency Selection

This section aims to identify forcing frequencies of highest potential for wake length reductions. While it may in fact be possible to force the wake with multiple superimposed waveforms of different frequency and type to achieve optimal performance, we restrict the study in this article to single frequency harmonic cases as described previously.

A frequency sweep was performed using a similar example case as described in Section III.C employing dynamic rotor frequency with a_f =0.02 rpm, $\omega_f = N_b(k - 0.5)$, and $\phi_f = 0°$. The instability growth for different forcing k are plotted in Figure 5(a). The best-fit slopes of the linear region between $1.0 \leq x/D \leq 1.4$ are the σ^* for each k, and these are compared in Figure 5(b) across all k.

Figure 5(b) depicts a clear trend in σ^* with peaks near integer k values and convergence of σ^* as k increases, both characteristics that are found for helices with small pitch in Widnall's [10] theoretical foundation on helical tip vortex instabilities. Furthermore, σ^* distributions of similar character, including a maximum growth rate at $k = 1$, have been observed by previous authors studying rotor configurations using both Fourier analyses [15, 17] and eigenvalue analyses [16, 21, 31]. The addition of the dynamic stall model tends to displace the σ^* curve to slightly higher k relative to the case without dynamic stall for k greater than roughly 1.5, though the location of maximum σ^*, $k = 1$, is unchanged with or without the model. In terms of absolute growth rates, this maximum σ^* is 1.41, or 10%, below the maximum theoretical value of $\pi/2$ for point vortices.

To further demonstrate the consistency of the Fourier result with other stability analysis techniques, an eigenvalue stability analysis for the unforced case on one blade's outer filament was performed following Bhagwat and Leishman's [16] formulation. The same fluctuating and decaying trends are seen in the eigenvalue result as the Fourier one, including the maximum growth rate at $k = 1$. Some differences compared to the Fourier result may exist since each method resolves slightly different targets; the eigenvalue analysis is applied directly to a single vortex filament while the Fourier analysis is calculated with velocities produced by the induction of all filaments in the flow field. Since the eigenvalue analysis is performed on an unforced wake, the eigenvalue result matches most closely with the Fourier result that does not include dynamic stall.

Illustrations of all three outer filaments are provided in Figure 5(b) for several k to aid in the causal analysis of the different growth rates. The graphics depict the effect of the various forcing frequencies on the outermost tip vortex filament emanating from each blade at an instant in time in the FVWM results. As in Figure 4(b) above, the absolute filament diameter does not possess meaning and is scaled for visual clarity. However, in Figure 5(b) and other figures to follow, the *relative* variation in filament diameter is indeed meaningful and represents changes in the magnitude of the local circulation produced by the filament (see the following section for discussion on local circulation changes for DWC cases). The filament circulation, as well as the axial and radial displacements of the filaments, relative to those of the unforced case are exaggerated by the factors given in the figure caption.

For the $k = 1.5$ illustration, adjacent filaments are displaced in-phase so that the DWC-induced displacements are only a function of azimuthal location in the domain regardless of which filament is being considered. The result is a

distortion of the whole helical structure, which makes each filament take on an "s"-shaped appearance as shown. The dynamic forcing thus has little impact on the streamwise spacing between adjacent filaments, and the $k = 1.5$ forcing therefore has a low growth rate. The same conclusions hold for larger, half-integer k values.

On the other hand, integer-valued k forcing cases displace adjacent filaments to be out-of-phase by 180° of the perturbation cycle. Tracking a single vortex filament for the $k = 1$ case, it can be observed that a filament pairs with an adjacent filament every 120° of azimuth, and the filament's pairing partner also alternates between every pairing position. For the $k = 2$ case, the pairing occurs every 80° of azimuth and again alternates between every pairing position. It could be said that the integer-valued forcing acts as a "matchmaker" between successive vortex filaments, prescribing the azimuthal location where two filaments will converge at instability hotspots. The $k = 1$ case will be used for all further results below because of its highest magnitude growth rate.

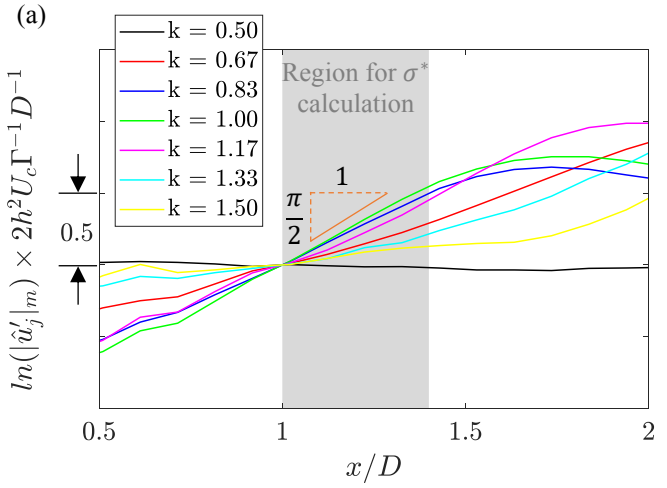

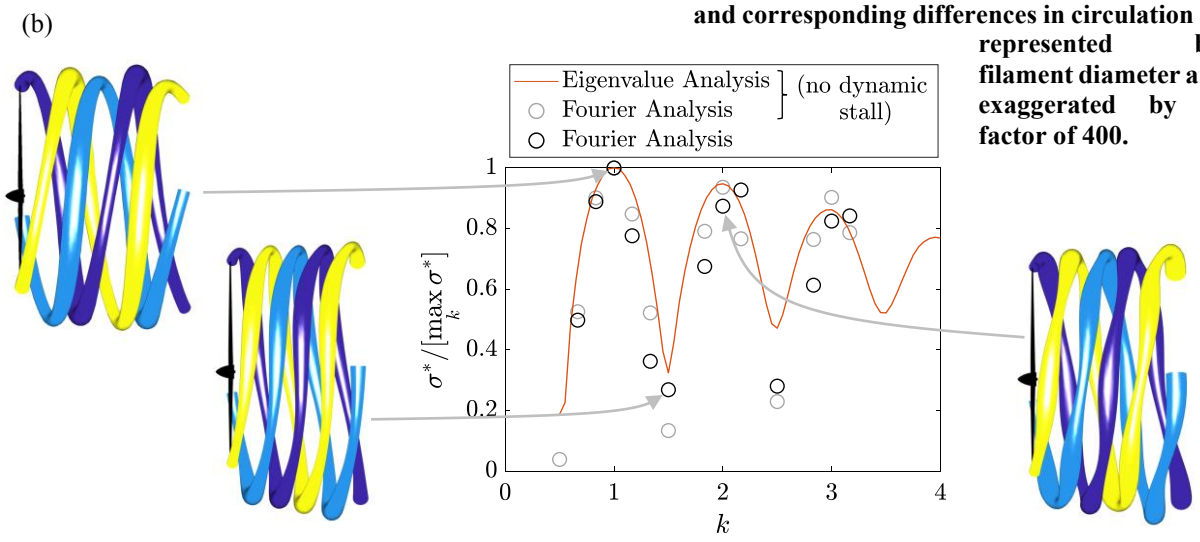

Figure 5. Instability growth for different frequency parameters, k, as applied by varying rotor frequency with $a_f = 0.02$ rpm, $\omega_f = N_b(k - 0.5)$, and $\phi_f = 0°$. (a) shows the scaled, non-dimensionalized, and smoothed maximum Fourier coefficients, $|\hat{u}'_j|_m$, aligned at the streamwise location, x/D, of 1 while (b) shows the scaled slopes calculated within the shaded region of (a). Comparison is made in (b) between the Fourier growth rates and the corresponding rates calculated with the eigenvalue approach on a tip vortex filament. For the illustrations of the three outer filaments in (b), axial and radial displacements of these filaments relative to the unforced case are exaggerated by a factor of 200 for clarity, and corresponding differences in circulation as represented by filament diameter are exaggerated by a factor of 400.

B. Amplitude Study

Figure 6 contains individual studies of rotor speed and pitching amplitude in the first two rows, respectively, and a tandem amplitude study in the third row. In each case, the amplitude sweeps of a_f and a_p show a clear trend of decreasing near-wake length with increasing forcing amplitude. For the tandem case in Figure 6(c), we began by selecting pairs of a_p and a_f based on similarity of $(x/D)_{nl}$ from the non-tandem results. For instance, the $a_p = 1.30°$ case from subfigure (b) is matched with the $a_f = 0.60$ rpm case from subfigure (a), corresponding to $(x/D)_{nl}$ of 0.65 and 0.64, respectively. As will be justified in the following section, the relative phase shift of the two forcing waveforms is set so that $\phi_f = 90°$ ahead of $\phi_p = 0°$. For the largest amplitude tandem case, the $|\hat{u}'_{j_1}|_m$ intersects the

non-linear threshold at the rotor plane, so this case may have negligible $(x/D)_{nl}$. As will be discussed in Section V, many of the cases in Figure 6 have the potential to shorten $(x/D)_{nl}$ relative to the turbulent near-wake lengths predicted by the model of Sørensen *et al.* [37].

The illustrations to the left of the plots depict the effect of the various DWC strategies on the tip vortex filaments at an instant in time in the FVWM results, and the same explanation of the illustrations as in Section IV.A again

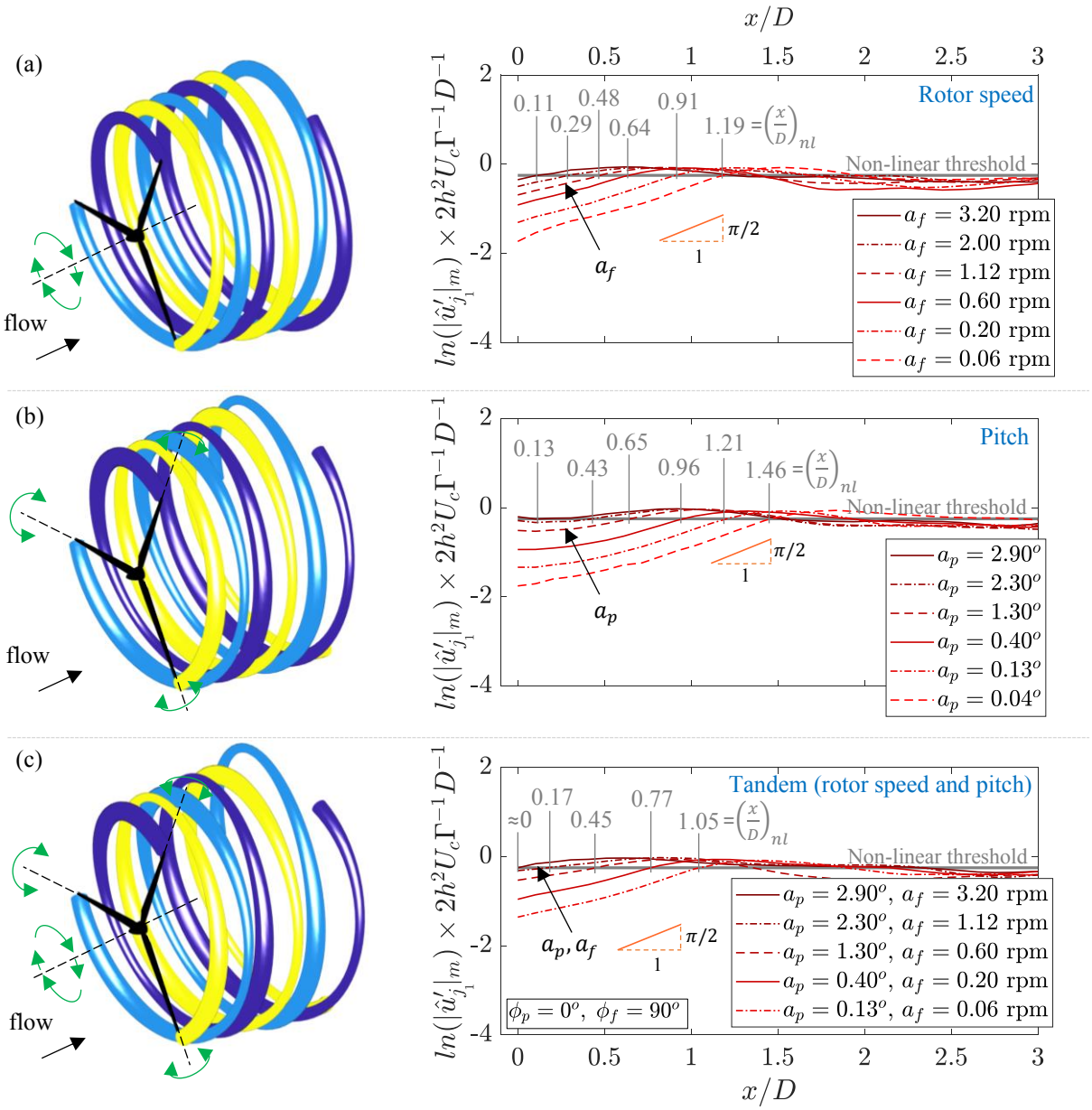

Figure 6. Left: Trajectory of the outermost tip vortex filaments taken for the first two revolutions downstream of the rotor at an instant in time from the FVWM results. Shown in (a), (b), and (c) are the a_f = 0.06 rpm, a_p =0.13°, and a_f = 0.06 rpm/a_p =0.13° cases, respectively, indicated on the right-hand plots. Axial and radial displacements of these filaments relative to the unforced case are exaggerated by a factor of 20 for clarity, and corresponding differences in circulation as represented by filament diameter are exaggerated by a factor of 40. Right: Demonstration of control authority over the initial maximum wake instability Fourier coefficients, $|\hat{u}'_{j_1}|_m$, as well as the growth along the streamwise coordinate, x/D. All cases use $\omega = 1.5$ ($k = 1$) and the harmonic amplitudes, a, and phase angles, ϕ, are zero unless noted otherwise. Lines are listed in the legend in the same order they appear vertically on the plots.

applies. The same observations about filament behavior as made for the a_f =0.02 rpm case with k =1 in Section IV.A hold for the a_f = 0.06 rpm, a_p = 0.13°, and tandem cases illustrated in Figure 6. The primary visual difference between the three cases is the size of the DWC-induced filament displacements, which correlates with the respective instability magnitudes plotted on the right-hand side of the figure. The $(x/D)_{nl}$ variations between cases are thus related to the filament displacements at the instability hotspots, which see the paired filaments of the tandem case coming closer together than for the individual cases, a visual confirmation that the tandem case achieves the strongest filament-pairing effect for the amplitudes considered. In fact, the beginning of the mutual inductance leapfrogging event can already be seen in the large displacements of the blue and purple filaments at the downstream limit of the plotted data in subfigure (c). A difference in circulation magnitude is also apparent between pairing filaments at the instability hotspots, especially in subfigures (b) and (c). Since the circulation magnitude between pairing filaments is 180° out of phase at any given azimuth, the mean circulation magnitude between any pair may be relatively constant.

It is relevant to note that the rate of instability growth within the linear region is the same to within a small percentage between all the cases in Figure 6 since the growth rate for a specific frequency of forcing is an inherent characteristic of the rotor wake [30]. Rather, it is the differences in the *initial amplitude* of the instability for each case that cause the non-linear regime to be reached at different x/D. For the cases involving dynamic pitch, the initial growth rate takes some stretch of distance to adopt a mutual inductance-type linear growth, though the dynamic forcing clearly still increases the initial instability magnitude, thereby shortening the near-wake length.

C. Phase Study

Figure 7 gives the results from the tandem configuration of a sweep of ϕ_f with constant ϕ_p. Varying the relative phase between the rotor speed and pitch forcing indicates a preferential phase shift of ϕ_f between 90-135° ahead of ϕ_p that produces the most constructive superposition of forcing waveforms and resulting reduction of $(x/D)_{nl}$. This trend is constant across the range of a_p amplitudes studied in Figure 7, though greater values of a_p for the given a_f clearly offer the greatest potential reduction of $(x/D)_{nl}$. For the largest a_p of 1.30°, the tandem result has a 30-31% lower $(x/D)_{nl}$ than either of the individual cases of the same forcing amplitudes.

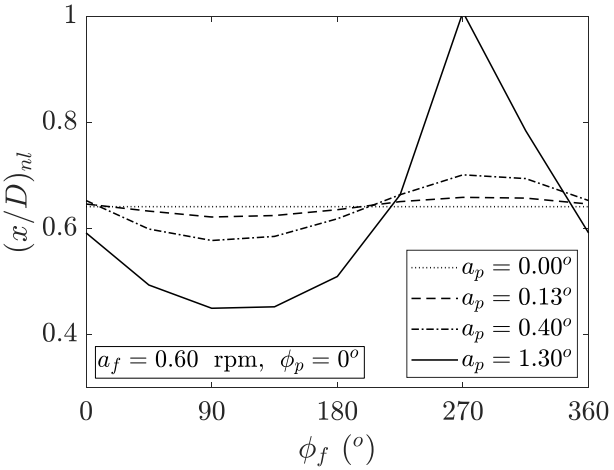

Figure 7. Effect of rotor speed forcing phase, ϕ_f, on near-wake length, $(x/D)_{nl}$ for a constant pitch forcing phase angle, ϕ_p. All cases use $\omega = 1.5$ ($k = 1$).

V. Analysis/Discussion

The above FVWM modeling does not consider the effects of atmospheric turbulence in the rotor inflow on instability growth. Inflow turbulence introduces perturbations to the tip vortex structures that may have an effect on wake instabilities that is comparable to the DWC actions studied above, depending on the turbulence intensity. The question becomes: how high can the turbulence intensity be for the DWC actions to still be effective?

The semi-empirical model of Sarmast *et al.* [9] incorporates a relationship between $(x/D)_{nl}$ and the inflow turbulence intensity, Ti, as in Equation 8

$$(x/D)_{nl} = 8\left[1 + C_2\left(\sqrt{1 - C_T} - 1\right)\right]^3 [N_b \lambda C_T]^{-1} \ln(C_1 Ti)\,, \tag{8}$$

where C_1 and C_2 are constants for which Sørensen *et al.* [37] found 0.33 and 0.52, respectively, C_T is the thrust coefficient taken as 0.756 from the FVWM results without DWC, N_b is the number of blades, and λ is the tip speed ratio. The equation is plotted in Figure 8 for reference.

The C_1 constant is furthermore useful as it is the constant of proportionality between a norm of the fluctuating axial velocity field, u'/U_∞, just behind the rotor blades and the corresponding Ti. In light of the derivation of Equation 8 that stems from the rotating sinusoidal axial tip forcing results of [17], one interpretation of u'/U_∞ is as the maximum

axial velocity Fourier coefficient magnitude computed in the rotating frame of reference just behind a blade. If it is assumed that the maximum Fourier coefficient in the calibration data used for C_1 was the maximum growth rate case of $k = 1$, then we may set u'/U_∞ equal to the value of $|\hat{\boldsymbol{u}}'_{j_1}|_m/U_\infty$ just behind the blades, which is conveniently already tabulated as a result of the above Fourier analysis. The proportionality relationship given in Sarmast *et al.* [9] and Sørensen *et al.* [37] could then be transcribed as $|\hat{\boldsymbol{u}}'_{j_1}|_m/U_\infty = C_1 Ti$. This relationship allows the addition of the DWC data from Section IV.B to Figure 8 where the value $[|\hat{\boldsymbol{u}}'_{j_1}|_m/U_\infty]/C_1$ on the horizontal axis may be considered the effective turbulence level associated with the DWC actions. The $|\hat{\boldsymbol{u}}'_{j_1}|_m$ is taken at the location $0.1D$ downstream from the rotor plane. Note that uncertainty in the value of C_1 due to the assumption of u'/U_∞ as the maximum Fourier coefficient manifests as uncertainty in the horizontal translation of the DWC data relative to the Sørensen *et al.* [37] line, though the slope of the data is not in doubt. The deviations of the DWC data from the semi-log linear slope of the Sørensen *et al.* model near the higher $|\hat{\boldsymbol{u}}'_{j_1}|_m/U_\infty$ may indicate that there are effects present in the current DWC flow fields that are not well described by the simple scaling between $|\hat{\boldsymbol{u}}'_{j_1}|_m$ and Ti proposed above.

The agreement of the tandem sweep curve with the individual sweep curves suggests that the tandem approach is not inherently superior to simply using an individual control vector with higher forcing magnitude, though structural quantities should also be investigated between the control vector approaches since $|\hat{\boldsymbol{u}}'_{j_1}|_m$ is at best a surrogate for some fluctuating thrust metric. Comparing the α_f sweep to the α_p sweep, the α_p sweep is "less efficient" than the α_f sweep in terms of the achieved $(x/D)_{nl}$ for a given input $|\hat{\boldsymbol{u}}'_{j_1}|_m$ over most of the range of $|\hat{\boldsymbol{u}}'_{j_1}|_m/U_\infty$ considered. This behavior may be understood in light of the slow initial growth of the pitch-induced instability discussed for Figure 6. The larger initial axial fluctuation magnitude of the dynamic pitch control approach could make this strategy more robust against the aperiodic interference of inflow turbulence, though much is still to be learned about the flow physics of the different DWC approaches. Initial analysis on the effectiveness of DWC in the presence of inflow turbulence is given next.

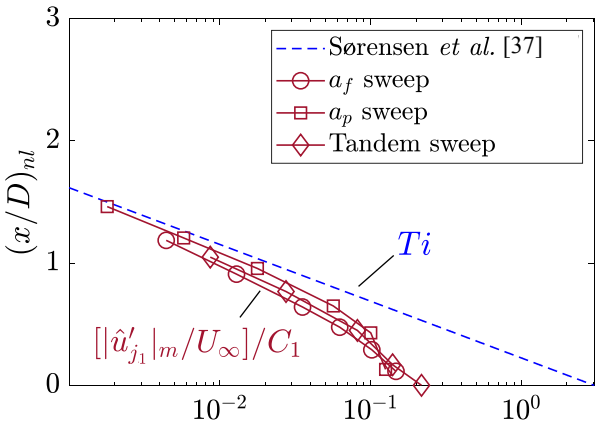

Figure 8. Near-wake length, $(x/D)_{nl}$, versus turbulence intensity, Ti, from Sørensen *et al.*'s [37] model (blue data) and scaled maximum axial perturbation magnitude, $[|\hat{\boldsymbol{u}}'_{j_1}|_m/U_\infty]/C_1$, as calculated $0.1D$ downstream of the rotor with DWC actions (red data).

From Figure 8, it is clear that some DWC actions of smaller magnitude will not reach their predicted $(x/D)_{nl}$ before high inflow turbulence environments would cause the wake to already begin to breakdown. For instance, $(x/D)_{nl} = 0.8$ according to Equation 8 for Ti =0.10 (10%), so the DWC actions of the lowest six $[|\hat{\boldsymbol{u}}'_{j_1}|_m/U_\infty]/C_1$ points plotted may have little effect on the $(x/D)_{nl}$ in such a case.

Figure 9 helps to visualize the potential benefit that different DWC magnitudes have on $(x/D)_{nl}$ by cross-referencing the $(x/D)_{nl}$ from the turbulent near-wake length model of Sørensen *et al.* [37]. The benefits in terms of relative $(x/D)_{nl}$ reductions are plotted versus the ratio of the perturbation magnitudes from the DWC to those from the inflow turbulence, $[|\hat{\boldsymbol{u}}'_{j_1}|_m/U_\infty]/[C_1 Ti]$. As this ratio increases, the likelihood increases that the DWC-applied waveform will be initially coherent and will remain coherent downstream, and thus the likelihood of the DWC actions to achieve the potential $(x/D)_{nl}$ reductions suggested by the non-turbulent FVWM results also increases. For all inflow Ti values, $(x/D)_{nl}$ reductions of over 80% are suggested for the maximum considered amplitude cases of a_f =3.20 rpm and a_p =2.90°. To limit fatigue on the active turbine, it might be advisable to use lower magnitude amplitudes. Specifically, dynamic rotor speed forcing with a_f =1.12 rpm, a value which is not large relative to naturally occurring rpm variation, could achieve 53% $(x/D)_{nl}$ reduction in a very stable atmosphere of Ti =0.02 (2%) and 43% $(x/D)_{nl}$ reduction in a more moderately stable atmosphere of Ti =0.05 (5%). Similar $(x/D)_{nl}$ reductions of 58% and 48%, respectively, are possible with dynamic pitch forcing of a_p =2.30°. As discussed above, the $[|\hat{\boldsymbol{u}}'_{j_1}|_m/U_\infty]$ stemming from dynamic pitch control generally have a higher margin relative to the turbulence than those from the dynamic rotor speed control for a given $(x/D)_{nl}$, at least for the axial perturbations considered here.

It should be noted that the minimum ratio $[|\widehat{\boldsymbol{u}}'_{j_1}|_m / U_\infty]/[C_1 Ti]$ for which DWC actions can still be effective is not known at this point, and thus conclusions about the potential for the DWC technique with lower magnitude forcing or at higher Ti conditions is unknown as well. Further high-fidelity modeling and/or measurements are necessary to establish firm estimates of the $(x/D)_{nl}$ reductions that DWC can offer in various turbulent environments. It can be summarized, however, that larger magnitude DWC actions are better both to yield potentially shorter $(x/D)_{nl}$ and higher likelihood of achieving the maximum benefits. On the other hand, fatigue damage and actuator wear also increase with the magnitude of dynamic turbine actions, and these consequences should also be the subject of future work.

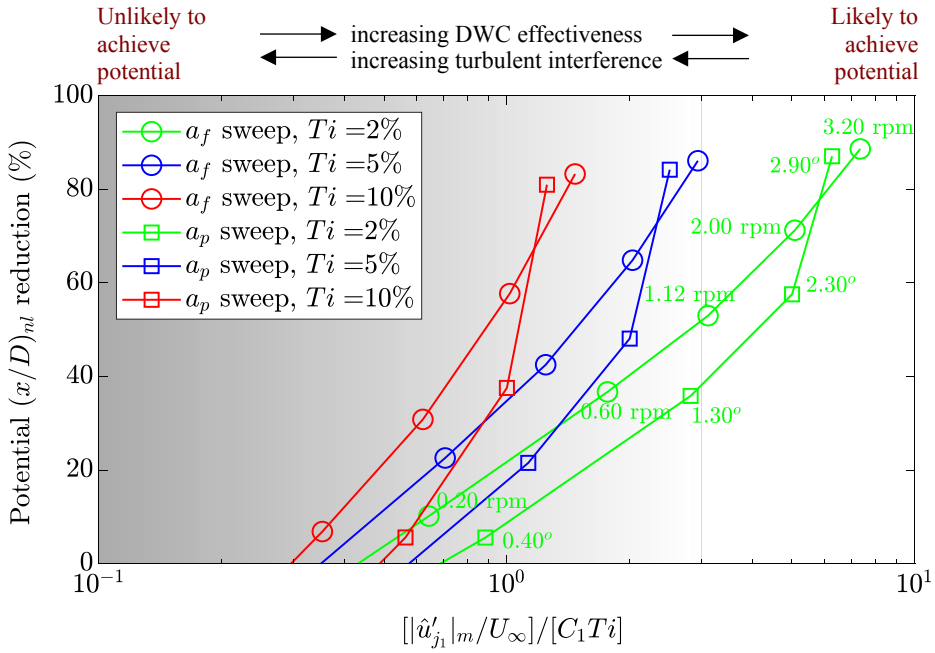

Figure 9. Potential reduction in near-wake length, $(x/D)_{nl}$, as a percent of the $(x/D)_{nl}$ from the turbulent near-wake length model of Sørensen *et al.* [37] versus likelihood of achieving the potential benefits with the DWC actions. The likelihood is quantified as the ratio of the maximum axial perturbation magnitude, $|\widehat{u}'_{j_1}|_m / U_\infty$, as calculated $0.1D$ downstream from the rotor plane in rotating frame-of-reference, to the scaled turbulence intensity, Ti. For visual clarity, the magnitudes of a_f and a_p are not annotated for the Ti =5% and Ti =10% cases, but these values follow the same sequences as annotated for the Ti = 2% cases.

VI. Conclusions and Outlook

The modified mid-fidelity FVWM code CACTUS is used to demonstrate the effectiveness of using dynamic rotor speed and blade pitch control to accelerate the breakdown of the near wake leading to a reduced overall wake length, and ultimately allowing turbine-to-turbine spacing to be reduced. Embedded in our approach is greater realism in the application of the dynamic control than in some previous work, as well as a focus on exciting the mutual inductance instability of the tip vortices rather than the bluff-body instabilities of the larger wake.

Stability analyses first confirmed that the harmonic forcing frequency parameter with the highest growth rate of the mutual inductance instability is $k = 1$, which corresponds to $\omega = 1.5$ for a three-bladed rotor. Using this frequency for parametric sweeps of the dynamic forcing amplitude of rotor speed, blade pitch, and tandem actions, $(x/D)_{nl}$ lengths of ≈0 to 1.46 were predicted over the range of rotor speed and blade pitch amplitudes considered. For the tandem cases, the phase difference between the forcing waveforms of the rotor speed and pitch was found to affect $(x/D)_{nl}$, and the most constructive superposition of waveforms occurred when ϕ_f =90-135° ahead of ϕ_p. Analyses that cross-referenced the DWC results with the turbulent near-wake length model of Sørensen *et al.* [37] indicated that $(x/D)_{nl}$ reductions of 48% with pitch forcing amplitude of $a_p = 2.30°$ are possible within a turbulent environment

of $Ti = 0.05$ (5%) and that similar $(x/D)_{nl}$ reductions of 43% are possible with rotor speed forcing of $a_f = 1.12$ rpm, a value which is not large relative to naturally occurring rpm variation. No inherent advantage of tandem control versus individual control vectors was immediately apparent, though both individual control vectors have unique upsides: rotor speed control produces no direct mechanical wear on the blade pitch system while blade pitch control may be more robust in the presence of inflow turbulence, though more investigation is required.

Additional work to be explored with the mid-fidelity FVWM approach include experimenting with different forcing waveform types (sinusoid, sawtooth, hybrids) and duty cycles. Cases could also include combined waveforms which are superpositions of multiple waveforms. Higher-fidelity simulations and/or measurements are next needed to pinpoint the efficacy of DWC in the presence of inflow turbulence, as well as to quantity the loading cost and turbine dynamics associated with the DWC approaches discussed above. Furthermore, the effect of DWC actions on the power production of the active turbine and validation of power increases in downstream turbines warrant further study.

Acknowledgments

This article was prepared by Sandia National Laboratories (SNL) Albuquerque, NM, 87185, U.S.A. SNL is a multi-mission laboratory managed and operated by National Technology and Engineering Solutions of Sandia, LLC., a wholly owned subsidiary of Honeywell International, Inc., for the U.S. Department of Energy's National Nuclear Security Administration under contract DE-NA-0003525.

The first author would like to thank Steven Rodriguez for his helpful discussions surrounding the eigenvalue stability analysis and numerical stability of FVWMs, in general. The first author also expresses thanks to Phil Chiu for his guidance on best practices for modifying the CACTUS code to include dynamic wake control actions, as well as to Christopher Kelley and Joshua Paquette for their reviews of the manuscript.

References

1. Zayas, J. *Wind Overview*. in *Sandia 2014 Wind Turbine Blade Workshop*. 2014. Sandia National Laboratories.
2. Nygaard, N.G. *Wakes in very large wind farms and the effect of neighbouring wind farms*. in *Journal of Physics: Conference Series*. 2014. IOP Publishing.
3. El-Asha, S., L. Zhan, and G.V. Iungo, *Quantification of power losses due to wind turbine wake interactions through SCADA, meteorological and wind LiDAR data.* Wind Energy, 2017. **20**(11): p. 1823-1839.
4. Herges, T., et al. *Detailed analysis of a waked turbine using a high-resolution scanning lidar*. in *Journal of Physics: Conference Series*. 2018.
5. Andersen, S.J., et al. *Comparison between PIV measurements and computations of the near-wake of an actuator disc*. in *Journal of Physics: Conference Series*. 2014. IOP Publishing.
6. Sorensen, J.N., et al., *Simulation of wind turbine wakes using the actuator line technique.* Philos Trans A Math Phys Eng Sci, 2015. **373**(2035).
7. Lignarolo, L., et al., *Tip-vortex instability and turbulent mixing in wind-turbine wakes.* Journal of Fluid Mechanics, 2015. **781**: p. 467-493.
8. Felli, M., R. Camussi, and F. Di Felice, *Mechanisms of evolution of the propeller wake in the transition and far fields.* Journal of Fluid Mechanics, 2011. **682**: p. 5-53.
9. Sarmast, S., et al., *Mutual inductance instability of the tip vortices behind a wind turbine.* Journal of Fluid Mechanics, 2014. **755**: p. 705-731.
10. Widnall, S.E., *The stability of a helical vortex filament.* Journal of Fluid Mechanics, 1972. **54**(4): p. 641-663.
11. Quaranta, H.U., H. Bolnot, and T. Leweke, *Long-wave instability of a helical vortex.* Journal of Fluid Mechanics, 2015. **780**: p. 687-716.
12. Sørensen, J.N., *Instability of helical tip vortices in rotor wakes.* Journal of Fluid Mechanics, 2011. **682**: p. 1-4.
13. Leishman, G.J., *Principles of helicopter aerodynamics with CD extra*. 2006: Cambridge university press.
14. Alfredsson, P.H. and J. Dahlberg, *A preliminary wind tunnel study of windmill wake dispersion in various flow conditions, part 7*. 1979: Stockholm, Sweden.
15. Marten, D., et al., *Predicting Wind Turbine Wake Breakdown Using a Free Vortex Wake Code.* AIAA Journal, 2020: p. 1-14.
16. Bhagwat, M.J. and J.G. Leishman, *Stability analysis of helicopter rotor wakes in axial flight.* Journal of the American Helicopter Society, 2000. **45**(3): p. 165-178.

17. Ivanell, S., et al., *Stability analysis of the tip vortices of a wind turbine.* Wind Energy, 2010. **13**(8): p. 705-715.
18. Tian, W. and H. Hu. *Effect of oncoming flow turbulence on the kinetic energy transport in the flow around a model wind turbine*. in *2018 Wind Energy Symposium*. 2018.
19. Yang, X., et al., *Coherent dynamics in the rotor tip shear layer of utility-scale wind turbines.* Journal of Fluid Mechanics, 2016. **804**: p. 90-115.
20. Hermsen, B.L., M. Bornemeier, and L. Luznik, *Near Wake Development Behind Marine Propeller Model in Presence of Freestream Turbulence.* Journal of Fluids Engineering, 2020. **142**(5).
21. Rodriguez, S.N. and J.W. Jaworski, *Toward identifying aeroelastic mechanisms in near-wake instabilities of floating offshore wind turbines.* Journal of Energy Resources Technology, 2017. **139**(5).
22. Kelley, C.L., D.C. Maniaci, and B.R. Resor. *Horizontal-axis wind turbine wake sensitivity to different blade load distributions*. in *33rd Wind Energy Symposium*. 2015.
23. Munters, W. and J. Meyers, *Towards practical dynamic induction control of wind farms: analysis of optimally controlled wind-farm boundary layers and sinusoidal induction control of first-row turbines.* Wind Energy Science, 2018. **3**(1): p. 409-425.
24. Yılmaz, A.E. and J. Meyers, *Optimal dynamic induction control of a pair of inline wind turbines.* Physics of Fluids, 2018. **30**(8): p. 085106.
25. Houck, D. and E. Cowen. *Can you accelerate wind turbine wake decay with unsteady operation?* in *AIAA Scitech 2019 Forum*. 2019.
26. Wang, C., et al. *Effects of dynamic induction control on power and loads, by LES-ALM simulations and wind tunnel experiments*. in *Journal of Physics: Conference Series*. 2020. IOP Publishing.
27. Odemark, Y. and J.H. Fransson, *The stability and development of tip and root vortices behind a model wind turbine.* Experiments in fluids, 2013. **54**(9): p. 1591.
28. Jonkman, J., et al., *Definition of a 5-MW reference wind turbine for offshore system development*. 2009, National Renewable Energy Lab.(NREL), Golden, CO (United States).
29. Jonkman, J. *DOWEC-NREL 5MW blade airfoil data-v2*. 2012; Available from: https://wind.nrel.gov/forum/wind/download/file.php?id=305&sid=5c5e9a9806fbb5667d0d3cf4383b2c4a.
30. Bhagwat, M.J. and J.G. Leishman, *Stability, consistency and convergence of time-marching free-vortex rotor wake algorithms.* Journal of the American Helicopter Society, 2001. **46**(1): p. 59-71.
31. Rodriguez, S.N., J.W. Jaworski, and J.G. Michopoulos, *Stability of Helical Vortex Structures Shed from Flexible Rotors.* arXiv preprint arXiv:2008.08969, 2020.
32. Branlard, E., et al. *Aeroelastic large eddy simulations using vortex methods: unfrozen turbulent and sheared inflow*. in *Journal of Physics: Conference Series*. 2015. IOP Publishing.
33. Kleusberg, E., S. Benard, and D.S. Henningson, *Tip-vortex breakdown of wind turbines subject to shear.* Wind Energy, 2019. **22**(12): p. 1789-1799.
34. Murray, J.C. and M. Barone, *CACTUS User's Manual.* Sandia National Laboratories, Albuquerque, NM, 2013.
35. Rodriguez, S.N., *Stability and dynamic properties of tip vortices shed from flexible rotors of floating offshore wind turbines*. 2018, Lehigh University.
36. Maniaci, D.C., *Wind turbine design using a free-wake vortex method with winglet application*, in *Aerospace Engineering*. 2012, Penn State.
37. Sørensen, J.N., et al. *Determination of wind turbine near-wake length based on stability analysis*. in *Journal of Physics: Conference Series*. 2014. IOP Publishing.